Chemical Science

ROYAL SOCIETY OF CHEMISTRY

EDGE ARTICLE

View Article Online
View Journal | View Issue

Cite this: *Chem. Sci.*, 2026, **17**, 6619

All publication charges for this article have been paid for by the Royal Society of Chemistry

Reactive lithium fluoride revitalizes bulk-interface Na-ion transport in all-solid-state PEO-based sodium batteries

You Fan,†[a] Binghong Zhao,†[a] Xin Zou,[a] Wenlong Zhao,[ac] Yanyan Zhang,[a] Meizhen Zhu,[a] Hong Zhang,[b] Zige Hong,[a] Xin Cheng,[a] Peiming Chen,[a] Zhengshuai Bai,*[a] Yanbin Shen[c] and Yuxin Tang*[ab]

Received 11th November 2025
Accepted 27th January 2026

DOI: 10.1039/d5sc08784h

rsc.li/chemical-science

Poly(ethylene oxide) (PEO)-based electrolytes suffer from low ionic conductivity and interfacial instability, which collectively impede their practical implementation in all-solid-state sodium metal batteries (ASSMBs). Conventional molecular-level strategies aim to enhance Na^+ conduction by regulating polymer chain organization; however, the strong covalent bonds formed thereby severely restrict the segmental motion critical for ion transport. Herein, we introduce reactive lithium fluoride to revitalize bulk Na^+ transport and interfacial stability simultaneously in solid-state PEO-based sodium batteries. The LiF-mediated supramolecular compound facilitates the formation of intrinsic anion-enriched aggregates and weakens Na^+-PEO coordination, thereby synergistically enhancing bulk Na^+ conductivity. Moreover, activated LiF *in situ* forms a dense, NaF-rich interfacial layer on the sodium anode surface, which homogenizes ion flux and suppresses dendritic growth. Consequently, the resultant electrolyte exhibits synergistic enhancements in ionic conductivity, mechanical robustness, and interfacial compatibility. The ASSMBs paired with a $Na_3V_2(PO_4)_3$ cathode demonstrate exceptional cycling stability, retaining 82.8% of the initial capacity after 400 cycles at 0.5C—markedly outperforming state-of-the-art polymer electrolyte-based ASSMBs. This study provides fundamental insights into the supramolecular functionalities of reactive fluorides, thereby offering a viable route to advance high-performance polymer-based ASSMBs.

Introduction

The pursuit of high-energy-density and safe energy storage systems has driven the rapid development of alkali metal batteries.[1,2] Compared to lithium-based counterparts, sodium metal batteries exhibit remarkable cost-effectiveness due to the natural abundance of sodium and superior low-temperature performance, positioning them as a promising candidate for next-generation energy storage.[3–5] However, the intrinsic flammability of traditional liquid electrolytes introduces substantial safety concerns, underscoring the critical necessity for transitioning to all-solid-state electrolytes (ASSEs).[6–8] Among all the ASSEs, PEO-based electrolytes have garnered substantial attention owing to their favorable interfacial compatibility, mechanical flexibility, and processability.[9,10] Despite these merits, PEO-based electrolytes suffer from intrinsic limitations, including ultralow ionic conductivity (10^{-6} to 10^{-5} S cm^{-1} at ambient temperature) and cation transference number (<0.3). These limitations give rise to pronounced concentration polarization effects both in the bulk electrolyte and at the electrolyte–electrode interfaces, which in turn facilitate the growth of sodium dendrites and promote polymer degradation, thereby compromising the overall electrochemical stability of the system.[11–13]

Molecular level strategies (*e.g.* grafting[1,14] or copolymerization[1,2,15]) can optimize the Na^+ conduction pathway within the bulk of solid-state electrolytes by regulating polymer chain arrangement. However, the formation of high-strength covalent bonds severely compromises the segmental mobility crucial for efficient ion transport.[16] In contrast, supramolecular-level strategies, characterized by dynamic bonding and synergistic effects, can be constructed under mild conditions and offer greater versatility in designing efficient lithium-conducting systems,[17] which have emerged as versatile tools for designing advanced solid-state electrolytes, leveraging dynamic and reversible non-covalent interactions (*e.g.*, hydrogen bonding, coordination bonding, and host–guest interaction) to balance ion transport efficiency and structural stability—advantages that covalent modification often lacks. Numerous

[a]*College of Chemical Engineering, Fuzhou University, Fuzhou 350116, P. R. China. E-mail: yxtang@fzu.edu.cn*

[b]*Qingyuan Innovation Laboratory, Quanzhou 362801, China*

[c]*i-Lab, Suzhou Institute of Nano-tech and Nano-Bionics, Chinese Academy of Sciences, Suzhou 215123, China*

† Y. Fan and B. Zhao contributed equally to this work.

supramolecular regulation approaches have been intensively investigated and comprehensively overviewed.[18] These supramolecular regulation methods have been widely explored in polymer electrolytes: hydrogen bonding enables reversible polymer chain crosslinking to enhance mechanical robustness while retaining segmental flexibility but is sensitive to moisture and limited in tuning ion coordination environments; coordination bonding (*e.g.*, metal–ligand interactions) modulates ion-polymer binding affinity to promote ion dissociation yet mostly focuses on single-ion regulation without synergistic optimization of bulk and interface properties; host–guest interactions construct ordered ion transport channels *via* macrocycle-based assemblies but face challenges in scalable fabrication and compatibility with high-capacity electrodes. Current supramolecular approaches primarily focus on integrating organic or inorganic additives into the electrolyte matrix.[19–23] As organic additives, plasticizers effectively suppress polymer crystallization by modulating supramolecular interactions, thereby facilitating ionic transport and mitigating polarization-induced dendrite growth.[19] Nevertheless, excessive suppression of chain entanglement often results in a significant reduction in mechanical integrity, a property critical for dendrite suppression. Conversely, rigid inorganic fillers (*e.g.*, inert oxides[24,25] or active ceramic particles[26,27]) can preserve mechanical robustness to physically block dendrite penetration. However, the inherent chemical mismatch and weak supramolecular interactions between inorganic fillers and polymers inevitably lead to interfacial incompatibility, ultimately causing long-term cycling instability.[28]

Beyond optimizing the bulk phase of electrolytes, interfacial compatibility between polymer electrolytes and electrodes remains a critical concern in ASSMBs.[29,30] At the anode side, inhomogeneous sodium deposition leads to the accumulation of dendritic "dead sodium", escalating interfacial resistance and short-circuit risks.[31] At the cathode side, the intrinsic electrochemical instability of PEO under high-voltage conditions triggers interfacial side reactions, yielding low-molecular-weight byproducts (*e.g.*, carboxyl and hydroxyl groups).[32] These byproducts compromise interfacial uniformity and impede ion transport *via* parasitic interactions with cations. Conventional *ex situ* molecular-level approaches (*e.g.* crosslinking[33] or end-capping[34] of polymer chains), while suppressing side reactions at the electrode–electrolyte interface, also restrict the mobility of the polymer matrix.

Furthermore, complex segmental topological structures and system compositions may introduce new interfacial compatibility challenges. Recent research efforts in solid-state batteries have targeted key bottlenecks such as poor interfacial stability, sluggish ionic transport, and volume expansion of high-capacity anodes. For instance, Zhang *et al.*[35] demonstrated that regulating interfacial chemistry of composite solid-state electrolytes can simultaneously boost ionic conductivity and interface stability, achieving long-cycle stability in lithium metal batteries *via* forming a stable solid electrolyte interphase (SEI). For silicon-based anodes—promising for high-energy solid-state batteries but plagued by huge volume variations—two complementary strategies have been reported: one focuses on manipulating charge-transfer kinetics alongside a flow-domain LiF-rich interphase to alleviate interfacial stress and stabilize cycling,[36] while a comprehensive review further highlights that addressing silicon's volume expansion and interfacial incompatibility is critical for practical application.[37] Beyond electrolyte and anode optimization, novel ionic conductors (*e.g.*, self-assembled hydrated copper coordination compounds) have also been developed to achieve high room-temperature ionic conductivity and electrode compatibility, providing new insights for solid-state electrolyte design.[38] However, most of these advances are either tailored for lithium-based systems rather than sodium-based counterparts or focus on single-aspect optimization (*e.g.*, only the interface or only the anode) without balancing bulk ionic transport and interfacial stability—two core requirements for practical ASSMBs.

In view of all the drawbacks of the conventional molecular-level approaches, a more effective supramolecular interaction system is needed to optimize bulk/interfacial ionic transport within the system. Inspired by reactive additives (*e.g.*, fluoroethylene carbonate, FEC) in liquid electrolytes, which synergistically regulate ion solvation structures and form stable electrode–electrolyte interphases *in situ*,[39] we propose a reactive fluoride-mediated strategy to revitalize bulk-interface Na-ion transport. Such fluorides can dynamically modulate bulk ion transport while enabling interfacial self-reconstruction *via* in situ-formed supramolecular compounds, thereby enabling dual optimization of electrochemical stability and mechanical robustness. Herein, as a proof-of-concept study, we incorporate reactive lithium fluoride (LiF) into PEO-based electrolytes for ASSBs. Characterized by chemical reactivity and electrochemical inertness in ASSMB systems, LiF functions *via* two synergistic supramolecular mechanisms: (1) its Lewis-acidic surface establishes stable supramolecular interactions with sodium salt anions, while the strong coordination capability of Li^+ weakens Na^+-EO coordination, thereby enhancing Na^+ dissociation and mobility;[40] (2) supramolecular interactions between LiF and PEO enhance lithium ion activity, thereby facilitating the electrochemical displacement reaction between LiF and sodium metal. This, in turn, promotes the *in situ* formation of a uniform NaF-rich solid-electrolyte interphase (SEI) and effectively suppresses dendrite propagation.[41–43] By constructing dynamic supramolecular bulk/interfacial interactions, this dual-functional design provides a paradigm for developing high-performance polymer-based ASSMBs through revitalizing bulk-interface Na-ion transport, emphasizing the critical role of supramolecular modulation in balancing ion transport and electrochemical stability.

Results and discussion

This study focuses on the mechanism and feasibility of reactive fluorides (taking LiF as a proof-of-concept model) as a supramolecular additive in poly(ethylene oxide) (PEO)-based ASSEs for ASSMBs. For PEO-based ASSEs, which consist of high-molecular-weight PEO and sodium trifluoromethanesulfonate (NaOTf), simultaneous optimization of bulk ion transport and interfacial stability is critical (Fig. 1a). The stability of ASSMB

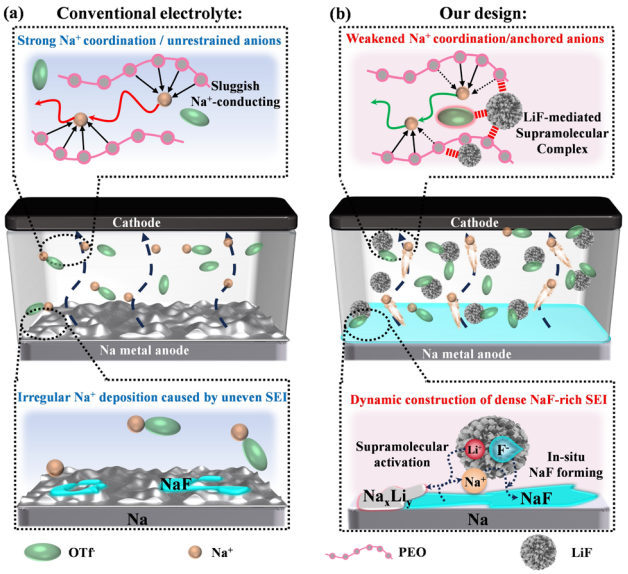

Fig. 1 Schematic illustrations of the challenges of (a) conventional PEO-based electrolytes and (b) concept of our design. By introducing reactive fluorides into the electrolyte, our design achieves supramolecular regulation of ion dissociation and Na^+ coordination environments in the bulk phase, while enabling dynamic formation of a uniform SEI layer through *in situ* replacement reactions at the sodium metal interface. This dual strategy significantly enhances both ion transport efficiency and cycling stability in the corresponding solid-state battery system.

systems is significantly compromised by concentration polarization, a consequence of low Na^+ migration efficiency in the electrolyte bulk. LiF addresses this critical issue by regulating ion migration asymmetry through the formation of supramolecular interactions. Owing to its extremely high lattice dissociation energy, Li^+ in LiF exhibits limited dissociation and thus does not participate in electrochemical (de)intercalation within the ASSMB system. However, surface-bound Li^+ on LiF particles dispersed in the electrolyte bulk can coordinate with oxygen atoms in adjacent ether chains *via* supramolecular transient dipole–dipole interactions. The ionic radius of Li^+ (0.076 nm) is substantially smaller than that of Na^+ (0.102 nm), endowing Li^+ with higher charge density and electronegativity, which in turn confers stronger coordination ability. In the LiF/PEO/NaOTf composite system, Li^+ leverages this strong coordination ability to preferentially occupy coordination sites on ethylene oxide (EO) chains, weakening Na^+-EO interactions and thereby promoting Na^+ migration. This argument is strongly supported by existing theoretical and experimental studies. Theoretical calculations by A. Vila *et al.*[44] on the binding enthalpies of Li^+/Na^+ with EO showed that the binding enthalpy of Li^+-EO complexes (-48.2 kJ mol^{-1}) is significantly lower than that of Na^+-EO (-33.1 kJ mol^{-1}), with a difference of 15.1 kJ mol^{-1}, indicating that Li^+ has a much stronger affinity for EO units and a lower dissociation energy, enabling it to preferentially occupy the coordination sites of EO in PEO matrices. Complementary experimental evidence comes from R. Andersson *et al.* [45] who quantified the coordination strength of Li^+/Na^+ with PEO using variable-temperature NMR spectroscopy. Their results demonstrated that the chemical shift change ($\Delta\delta$) induced by Li^+-PEO coordination (0.87 ppm) is nearly twice that of Na^+ (0.42 ppm), directly confirming that Li^+ forms more stable coordination complexes with EO units in practical polymer electrolyte systems, which is consistent with the proposed low dissociation energy characteristic of Li^+. Further density functional theory (DFT) calculations by B. Keshav Rao *et al.*[46] on PEO-LiI/NaI systems revealed the intrinsic structural basis for this coordination preference: Li^+ forms shorter Li^+–O bonds (1.92 Å) with EO oxygen atoms compared to Na^+ (2.34 Å), and the interaction energy of Li^+ with PEO (-2.87 eV) is lower than that of Na^+ (-2.13 eV), meaning that Li^+-EO coordination is more thermodynamically stable and less likely to dissociate. This electronic and structural analysis further validates that Li^+ can outcompete Na^+ for EO coordination sites due to its inherent properties. Additionally, fluoride ions (F^-), due to their high electronegativity, interact electrostatically with triflate anions (OTf^-), effectively anchoring OTf^- to reduce their mobility. Collectively, these dual mechanisms—F^--mediated OTf^- immobilization and Li^+-driven weakening of Na^+-EO interactions—enable balanced ion migration and suppressed polarization (Fig. 1b). Additionally, fluoride ions (F^-), due to their high electronegativity, interact electrostatically with triflate anions (OTf^-), effectively anchoring OTf^- to reduce their mobility. Collectively, these dual mechanisms—F^--mediated OTf^- immobilization and Li^+-driven weakening of Na^+-EO interactions—enable balanced ion migration and suppressed polarization (Fig. 1b).

Beyond its role in optimizing sodium-ion migration efficiency through supramolecular modulation within the polymer electrolyte, the specific interaction of LiF with the sodium anode further facilitates the reconstruction of electrode/electrolyte interfaces. On the Na^+ anode side, LiF mitigates dendrite formation through interfacial engineering: a spontaneous displacement reaction between LiF and Na generates a sodium fluoride (NaF)-rich solid electrolyte interphase (SEI), which homogenizes Na^+ flux and inhibits dendrite growth. On the cathode side, PEO-coordinated Li^+ ions remain electrochemically inert within the operating voltage window of sodium vanadium phosphate (NVP), as the lithium intercalation potential significantly exceeds that of Na^+.[47,48] This electrochemically inert state of Li^+ not only weakens Na^+-EO coordination but also passivates vulnerable ether bonds and hydroxyl groups through supramolecular binding, thereby enhancing the electrolyte's oxidative stability (Fig. 1b). By synergistically optimizing bulk ion transport, stabilizing anode interfaces, and improving cathode compatibility, LiF embodies a bidirectional supramolecular modulation strategy for PEO-based electrolytes. Its multifunctionality—encompassing anion anchoring, coordination competition, *in situ* SEI formation, and electrochemical stabilization—highlights its strong potential for high-performance, dendrite-resistant ASSMBs.

To verify this proposed advantage of LiF, we prepared ASSEs containing LiF as a multifunctional additive *via* solution casting, denoted as L-PEO. The LiF content was optimized to 5% following comprehensive evaluation of key parameters

including dispersion, membrane mechanical properties, and interfacial impedance. Elemental distribution uniformity in L-PEO was confirmed *via* EDS mapping (Fig. S1), with the mapping results revealing a relatively uniform elemental distribution, confirming good dispersion of the additive within the electrolyte bulk. To clarify the specific role of LiF, control polymer electrolyte membranes were prepared following the same protocol with either 5% NaF or no fluoride additive, denoted as S-PEO and P-PEO, respectively. Top-view and cross-sectional scanning electron microscopy (SEM) images of P-PEO, L-PEO, and S-PEO (Fig. S2a–f) indicate that the introduction of LiF or NaF does not alter the polymer electrolyte's surface morphology or its ~70 μm film thickness. Meanwhile, SEM images of LiF and NaF particles are shown in Fig. S3.

It is generally accepted that the introduction of fillers into all-solid-state polymer electrolytes disrupts the orientational arrangement of PEO segments through the formation of new interfacial interactions, which weaken interchain hydrogen bonds or dipole interactions. The disruption of PEO's crystalline structure further leads to an increase in the amorphous region fraction, reduces the energy barrier for segmental motion, and causes a downward shift in the glass transition temperature (T_g).[49] Concurrently, decreased crystallinity and reduced crystalline domain size induce a downward shift in the melting temperature (T_m) and lead to a substantial reduction in the integrated area of the melting peak. However, as shown in the differential scanning calorimetry (DSC) curve in Fig. S3, the T_g peak position of PEO-based polymer electrolytes with NaF and LiF additives remains largely unchanged compared to P-PEO. This indicates that fluoride introduction has a limited effect on the mobility of polymer segments. Meanwhile, although both L-PEO and S-PEO exhibit a noticeable decrease in T_m relative to P-PEO, further comparison of integrated melting peak areas reveals no significant reduction in the crystallinity of PEO segments within the electrolyte.

This phenomenon contradicts the typical crystallization-suppressing effect of conventional fillers. Considering the potential mechanisms of reactive fluorides, this discrepancy can be attributed to the following aspects: firstly, the T_g of a polymer indirectly reflects the flexibility and mobility of its molecular chains. Unlike plasticizers, fluoride particles influence the system's crystallization behavior primarily by favoring "random aggregation" over "ordered crystallization". This process disrupts the original interchain entanglement of PEO while establishing new interactions among fluorides, polymers, and sodium salts. Owing to these newly formed intermolecular interactions, the molecular mobility of PEO does not significantly improve upon fluoride incorporation. Secondly, beyond direct bonding with polymer segments, fluorides can also act as heterogeneous nucleation promoters to modulate the crystallization behavior of PEO segments. This directly leads to the formation of numerous "incomplete" crystalline regions (characterized by abundant defects with broader full width at half maximum of the melting peak; details can be found in the SI) within the bulk polymer electrolyte. According to the Thomson–Gibbs equation (see details in the SI), the emergence of such "incomplete" crystalline regions—though not necessarily reducing the system's overall crystallinity—can significantly lower its T_m, a trend consistent with the observed changes in crystallization behavior upon adding reactive fluorides. Further analysis of the DSC curves for P-PEO, S-PEO, and L-PEO (Fig. 2a) reveals that each melting peak can be deconvoluted into two components: region A (around 61 °C), corresponding to small, defect-containing partially crystallized PEO domains (*i.e.*, crystalline regions exhibiting lattice irregularities and thin-layered structures), and Region B (near 64 °C), corresponding to large-sized, orderly arranged PEO crystalline domains (defect-free, closely packed lattice structures with thick-layered structures). In P-PEO, the intensity of Region A is significantly lower than that of Region B, indicating a high degree of structural regularity in PEO chain packing in the absence of fluoride additives. With fluoride introduced, however, the system exhibits marked crystalline disorder, evidenced by the notably increased proportion of Region A in the DSC curves. This can be ascribed to the newly formed intermolecular interactions and heterogeneous nucleation effects discussed earlier. Furthermore, the proportion of Region A in L-PEO is slightly lower than that in S-PEO, possibly arising from stronger interactions between LiF and polymer chains or sodium salt anions. Consequently, the compounds formed in L-PEO are more compact than those in S-PEO, and such dense packing contributes to improved crystalline integrity. In summary, thermal analysis of P-PEO, S-PEO, and L-PEO suggests that fluoride additives participate in the formation of new interaction networks within the bulk electrolyte. These interactions persist even above T_m and are expected to impact the ionic transport efficiency of the entire electrolyte system.

The XRD patterns of P-PEO, S-PEO, and L-PEO are presented in Fig. 2b. Notably, the characteristic peaks of NaF and LiF are clearly distinguishable in S-PEO and L-PEO, respectively. All three samples exhibit distinct diffraction peaks at approximately 19.2° and 23.4°, corresponding to the (120) and (112) planes of crystalline PEO.[50] This indicates that the added fluorides did not induce the formation of new crystalline structures through chemical reactions within the system. Further analysis of the integrated intensity ratio between the (120) and (112) diffraction peaks revealed that L-PEO exhibits a more pronounced (120) plane orientation compared to P-PEO and S-PEO, as illustrated by the statistical results in Fig. S4. In the crystalline regions, PEO chains adopt a 7/2 helical conformation (two helical turns per seven repeating units).[51] The (120) plane, parallel to the helical chain axis, reflects the lateral stacking distance between adjacent chain bundles ($d \approx 4.63$ Å), whereas the (112) plane corresponds to a tighter, cross-stacked arrangement of neighboring chains ($d \approx 3.86$ Å).[52] Owing to its stronger interaction with PEO chains, LiF provides more effective heterogeneous nucleation sites and exhibits better lattice matching with the (120) plane, thereby promoting a more distinct (120) orientation in PEO. The enhanced prevalence of the (120) plane—characterized by a larger interplanar spacing and alignment parallel to the primary ion migration direction (along the chain axis)—significantly contributes to improving the ion transport efficiency of the electrolyte system.

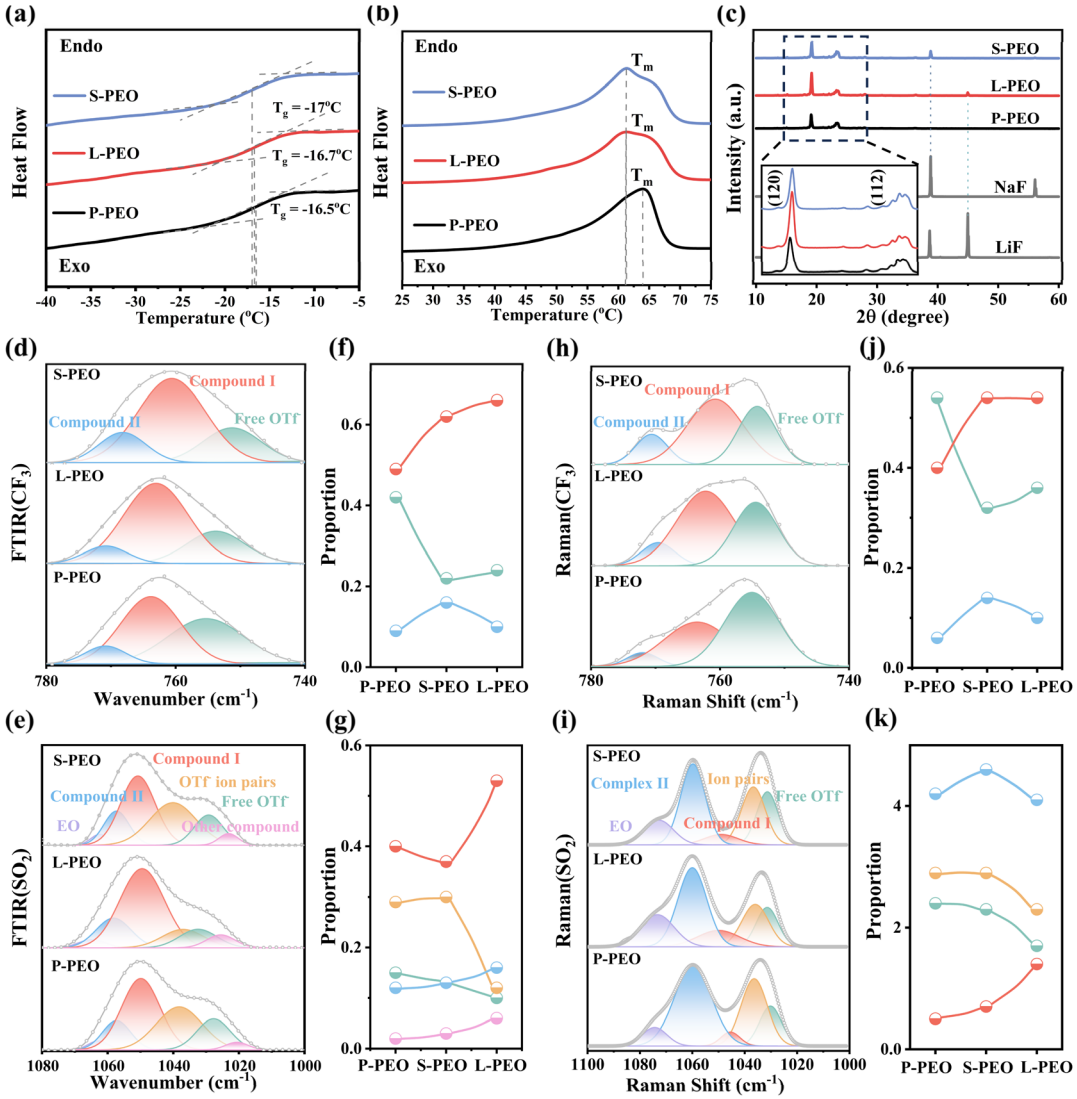

Fig. 2 Characterization of crystallization behavior, mechanical properties, and spectral characteristics of P-PEO, L-PEO and S-PEO. DSC curves of P-PEO, L-PEO and S-PEO in the temperature range of (a) −40∼−5 °C and (b) 25∼75 °C. (c) XRD patterns of LiF, NaF, P-PEO, L-PEO and S-PEO. The FTIR spectrum of P-PEO, L-PEO and S-PEO at (d) 740∼780 cm^{-1} and (e) 1000∼1080 cm^{-1} with corresponding peak proportion comparison summarized in (f) and (g) respectively. The Raman spectrum of P-PEO, L-PEO and S-PEO at (h) 740∼780 cm^{-1} and (i) 1000∼1100 cm^{-1} with corresponding peak proportion comparison summarized in (j) and (k), respectively.

The crystallization behavior of polymer electrolytes is associated with the stacking morphology of multiple components, which not only affects ion migration efficiency but also influences the electrolyte's surface morphology, mechanical properties, and long-cycling stability (specifically, dendrite suppression capability) of the system. 3D reconstructed AFM images of the as-prepared PEO-based electrolyte membranes are presented in Fig. S5, depicting the surface topographies of P-PEO, L-PEO, and S-PEO. Modulated by intermolecular interactions and crystallization behavior, the incorporation of LiF and NaF significantly reduces the roughness of the electrolyte membranes. Reduced roughness minimizes the scattering and hindrance of electrons and ions at the electrolyte surface, thereby lowering resistive losses. This, in turn, improves interfacial contact efficiency, mitigates localized reactions, enhances surface uniformity, and reduces leakage risks, among other benefits. To evaluate the effect of fluorides on the mechanical properties of ASSEs, tensile and puncture stress–strain tests were conducted. As shown in Fig. S6a, owing to the inherent rigidity of fluorides and the "fluoride-PEO-OTf^-" interactions formed within the system, the tensile properties of S-PEO and L-PEO were enhanced relative to P-PEO (yield stress: 11.4 MPa; elongation at break: 739.5%). The improved tensile strength aids in suppressing sodium dendrite growth and mitigating the risk of short circuits. Puncture tests (Fig. S6b) demonstrated that P-PEO withstood a puncture force of 1.9 N at a displacement of 4.3 mm. In comparison, L-PEO withstood 2.3 N at 3.9 mm displacement, while S-PEO exhibited significantly higher puncture resistance (3.6 N) at a smaller displacement of only 2.1 mm. The Young's modulus of pristine P-PEO is

~2.1 MPa, while that of LiF-modified L-PEO reaches ~3.5 MPa, representing a 67% enhancement. These enhancements aid in preventing sodium dendrites from penetrating the electrolyte, thereby avoiding internal short circuits and thus contributing to improved cycling stability and safety.

The altered crystallization behavior of Na^+-conducting backbone segments in polymer electrolytes necessarily induces concurrent changes in the arrangement of other system components. Thus, while fluorides affect the characteristics of PEO crystalline domains, they also inevitably influence the aggregation behavior of sodium salts (Na^+ and OTf^-) and their interactions with PEO segments—factors critical to Na^+ conduction, which were further characterized *via* FTIR and Raman spectroscopy. Fig. S7 presents the infrared spectra of P-PEO, S-PEO, and L-PEO. All three electrolytes exhibit the strongest peak from PEO chains at 1000.0~1200.0 cm^{-1}; however, fluoride additives did not induce significant spectral changes. To investigate their impact on OTf^-/PEO interactions, fine-scan adjustments within this range and peak fitting analysis of the results are required. Fig. 2d and h display FTIR and Raman spectra of P-PEO, S-PEO, and L-PEO in the 740.0~780.0 cm^{-1} region. As indicated by Table S2 and Fig. 2d, the -CF3 FTIR and Raman signals of ASSEs can be deconvoluted into three peaks, assigned to free OTf^-, Compound I (PEO-OTf^- interactions), and Compound II (PEO-OTf^--Na^+ interactions).[53] Compared to P-PEO, the introduced LiF reduces the proportion of free ions and ion pairs in the electrolyte film while increasing those of Compounds I and II (Fig. 2f and j). In this system, LiF interacts with free PEO segments or PEO-OTf^-, immobilizing more OTf^- within the crosslinked polymer backbone. This releases free Na^+ and disassembles large compounds into smaller ones, facilitating Na^+ migration. The Raman spectra in the same region (Fig. 2h) show a consistent trend, confirming these observations. Fig. 2e and i show FTIR and Raman spectra of the samples in the 1000.0~1100.0 cm^{-1} range (symmetric stretching of $-SO_2^-$ in OTf^-). As evident from Table S3 and Fig. 2d, LiF addition reduces free ions/ion pairs and increases Compound I, Compound II, and free PEO segments compared to P-PEO, consistent with the above trend. Notably, in Fig. 2k, the peak intensity of Compound II is significantly higher than that of Compound I for all samples, contradicting Fig. 2g. This discrepancy arises from intermolecular interactions affecting the $-SO_2^-$ symmetric stretching intensity in different compounds. According to Raman and infrared principles, Raman spectroscopy is more sensitive to symmetric vibrational signals. In Compound I, PEO-OTf^- interactions restrict OTf^--related bond vibrations and symmetry; in Compound II, Na^+ involvement weakens PEO-OTf^- interactions, enhancing $-SO_2^-$ symmetric vibrational signals. In summary, LiF immobilizes OTf^- within the crosslinked backbone by interacting with free PEO segments or PEO-OTf^-, releasing free Na^+ and disassembling large compounds, thereby facilitating Na^+ migration—consistently supported by the FTIR and Raman results.

Heterogeneous nucleation crystallization and bulk-phase aggregation behavior in polymer electrolytes effectively promote sodium salt dissociation and ion migration, thereby exhibiting significant potential for rate performance and electrochemical stability in ASSMBs. Solid-state NMR was utilized to assess Na^+ mobility in various PEO-based polymer electrolytes. Fig. S8a and b present the solid-state NMR spectra of P-PEO, L-PEO, and S-PEO. The ^1H NMR spectra of these electrolytes display two distinct signals. In this study, the solid-state electrolyte system is designed with a large excess of EO units (EO : Na = 20 : 1). For P-PEO, the major peak at 3.02 ppm corresponds to methylene protons adjacent to ether bonds uncoordinated with metal ions, while the low-field peak at 3.16 ppm arises from protons near coordinated ether oxygens—consistent with the deshielding effect from metal ion coordination. S-PEO exhibits no significant changes in peak intensity or chemical shift relative to P-PEO. For L-PEO, however, the low-field signal undergoes a more pronounced upfield shift to 3.21 ppm (the main peak position remains unchanged), attributed to LiF-induced strengthening of the coordination environment.

The ^{23}Na NMR spectra reveal that P-PEO exhibits a signal at −0.376 ppm, whereas LiF addition causes a downfield shift to −0.357 ppm with increased peak separation. This indicates weakened Na^+-EO binding affinity, facilitating the liberation of free Na^+. This phenomenon can be explained as follows: In P-PEO, strong interactions exist between PEO and Na^+, forming a binary blend system of PEO and NaOTf within the electrolyte. LiF introduction enables Li^+ to compete with Na^+ for PEO coordination sites, weakening PEO-OTf^--Na^+ interactions and releasing more free Na^+ ions. In contrast, in the absence of Li^+, S-PEO shows no significant chemical shift variation. Fig. S9a demonstrates the increased ionic conductivity by LiF addition. At 65 °C (operating temperature), L-PEO and S-PEO exhibit comparable ionic conductivities (3.1×10^{-5} and 3.7×10^{-5} S cm^{-1}, respectively), both significantly higher than that of P-PEO (9.6×10^{-6} S cm^{-1}). Furthermore, owing to LiF-induced anion immobilization and bulk-phase coordination modulation, L-PEO exhibits a higher Na^+ transference number than S-PEO and P-PEO (Fig. S9b). Thus, combining the ionic conductivity and transference number results, L-PEO shows significantly improved ion migration efficiency.

Beyond regulating intermolecular interactions and coordination environments in the bulk phase, reactive fluorides also beneficially optimize electrode–electrolyte interfaces. Influenced by the metal activity sequence, Li^+ from LiF will be reduced by the Na anode, together with the production of NaF. Such *in situ* displacement reactions at the Na metal anode-electrolyte interface markedly influence SEI composition and dendrite suppression. To clarify the mechanism of fluoride-mediated interface regulation, X-ray photoelectron spectroscopy (XPS) with argon ion sputtering was utilized to characterize Na‖NVP batteries assembled with distinct electrolytes. Fig. 3 presents XPS depth profiles of cycled Na anode surfaces, enabling detailed analysis of post-cycling Na metal surface composition. All peak positions were calibrated against the C 1s peak at 284.8 eV. High-resolution C 1s spectra of P-PEO, L-PEO, and S-PEO confirm C–C (284.8 eV), ether (C–O, 286.7 eV), carboxyl (O–C=O, 289.5 eV), and $-CF_3$ (292.3 eV) groups.[38] Notably, residual surface electrolyte was thoroughly removed with ultra-dry solvent prior to XPS, so C 1s signals originate

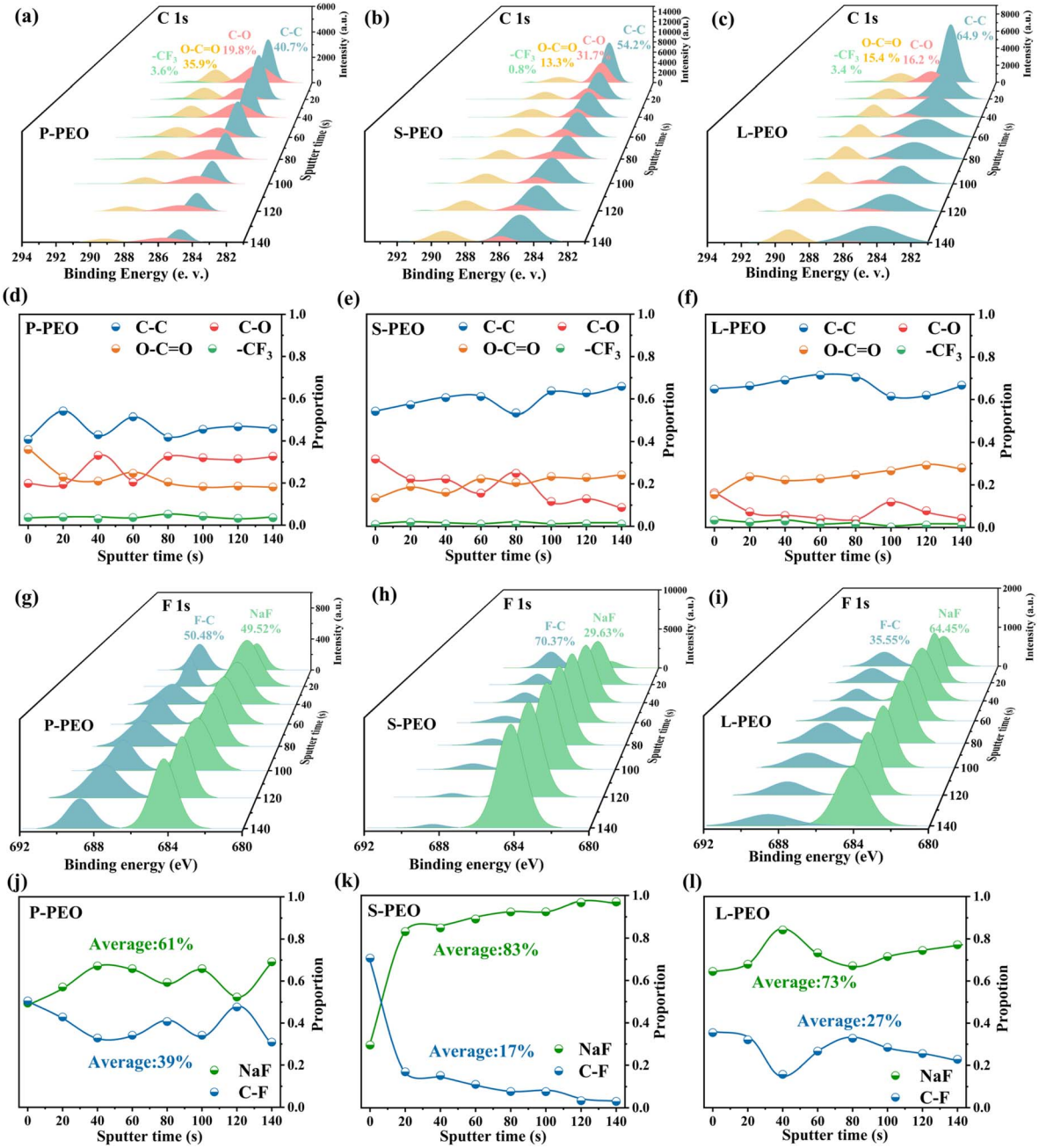

Fig. 3 The high-resolution fitted (a)–(c) C 1s and (g)–(i) F 1s XPS depth (etching time) analysis of the cycled Li electrodes compared with those of (a), (g) P-PEO, (b), (h) S-PEO and (c), (i) L-PEO. (d)–(f) The corresponding peak proportion comparison of C–C, C–O, O–C=O and $-CF_3$. (j)–(l) The corresponding peak proportion comparison of C–F and NaF.

solely from (i) SEI components derived from PEO and OTf^- anion decomposition and (ii) undecomposed polymer segments strongly interacting with the anode surface. Comparison of C 1s signals reveals lower ether and carboxyl group proportions in L-PEO than in P-PEO and S-PEO, indicating that LiF-PEO bulk interactions and interfacial protective layer formation significantly inhibit polymer segment decomposition. More importantly, C–O signal evolution with etching depth differs markedly among the three systems (Fig. 3d–f). Unlike P-PEO and S-PEO, where C–O signals decay slowly with increasing etching depth, L-PEO exhibits a sharp C–O signal reduction after only 20 s of etching. This distinction arises from differing origins of surface C–O signals: in L-PEO, stronger LiF-PEO interactions drive increased PEO adsorption on the Na surface; the high steric hindrance of undecomposed PEO segments prevents deep SEI penetration, causing rapid signal attenuation with etching. In contrast, P-PEO and S-PEO lack such strong segment interactions, so C–O signals predominantly derive from decomposed PEO/OTf^- products—smaller steric hindrance enables deep SEI

penetration, leading to gradual signal decay. This confirms that LiF inhibits interfacial PEO decomposition in L-PEO.

High-resolution F 1s spectra (Fig. 3g–i) confirm C–F (688.8 eV) and metal fluoride (684.8 eV) species.[38] Driven by *in situ* surface displacement, L-PEO exhibits enhanced NaF formation on the Na anode; increased NaF endows the SEI with higher mechanical strength and Na^+ transport efficiency. Furthermore, L-PEO shows minimal F content variation across the SEI (Fig. 3j–l), whereas P-PEO and S-PEO display larger fluctuations—indicating that LiF improves SEI compositional homogeneity, ensuring uniform ion transport and mechanical properties for sustained dendrite suppression.[54] Notably, the NaF-added electrolyte (S-PEO) did not markedly enhance surface NaF content in the SEI. Although deeper etching reveals increased NaF in S-PEO, excessive NaF elevates SEI brittleness and sharp compositional gradients disrupt ion transport pathway uniformity—both detrimental to long-cycle stability.[17] In conclusion, LiF is capable of suppressing polymer segment decomposition by constructing a "buffer layer" with supramolecular compounds at the anode-electrolyte interface, which can be further confirmed by LSV (Fig. S10a) and electrochemical floating (Fig. S10b) tests. Meanwhile, the dense and uniform NaF-rich SEI formed *via* the *in situ* displacement reaction promotes stable ion conduction, collectively enabling robust Na metal cycling.

The XPS depth profiles show that the introduction of LiF plays a crucial role in dynamically regulating the composition of the anode-electrolyte interface. Building on this insight, we further visualized the distribution of fluoride-rich supramolecular compounds at the interface using ToF-SIMS to investigate the chemical evolution of the *in situ* formed SEI. Fig. 4a and d present 3D renderings of NaF and F^- distributions at the Na/ASSE interface after battery cycling, alongside ToF-SIMS F^- mapping images and depth profiles of the various compositions formed at the Na/ASSE interface, as shown in Fig. 4b, c, e and f, respectively (corresponding mass spectra of the samples are provided in Fig. S11). ToF-SIMS 3D volume renderings directly confirm the most critical feature of NaF distribution: a continuous, non-agglomerated network at the L-PEO/Na interface, with no isolated fluoride clusters or voids observed. This exceptional uniformity (both lateral and vertical) originates from two interconnected mechanisms unique to LiF modification: the *in situ* displacement reaction between LiF and the Na anode ($Na + LiF \rightarrow NaF + Li^+$), which drives NaF formation directly on the electrode surface, and the supramolecular interactions (Li^+-EO coordination and F^--OTf^- attraction) that guide ordered NaF nucleation and growth. This stands in stark contrast to the P-PEO system, where phase separation is prevalent due to the lack of such regulatory effects, resulting in uneven, agglomerated NaF domains. Beyond uniformity, ToF-SIMS depth profiling further reveals two other key structural features of the NaF layer: well-defined optimal thickness and the absence of a concentration gradient. The NaF layer exhibits a moderate, well-controlled thickness that strikes a critical balance between mechanical robustness and interfacial ion transport efficiency—sufficiently thick to act as a physical barrier against dendrite penetration (leveraging NaF's high Young's modulus) while avoiding excessive interfacial resistance that would impede Na^+ transport. Additionally, the F^- signal intensity remains consistent across the entire NaF layer, indicating a gradient-free concentration distribution that eliminates localized Na^+ accumulation, a major trigger for uneven Na deposition and dendrite nucleation.

Finite element analysis (FEA) has emerged as an increasingly powerful numerical tool employed to unravel the intricate mechanisms of dendrite nucleation and growth in PEO-based electrolytes, thus facilitating system optimization and interface design. Fig. 4g–i illustrate the potential distribution derived from FEA simulations. Specifically, P-PEO exhibits the lowest ionic diffusivity and mobility, lacks a protective layer, and undergoes uneven Na deposition—ultimately leading to elongated dendrite formation. In contrast, S-PEO demonstrates superior ionic diffusivity and mobility, enabling more uniform Na deposition than P-PEO. For L-PEO, however, the presence of a protective layer, combined with favorable ionic diffusivity and mobility, results in the most uniform Na deposition and ion distribution, with virtually no dendrite formation. These observations are further supported by the concentration field distributions from FEA (see Fig. S12). Consistent with these findings, the potential distribution analysis reveals that P-PEO exhibits the most uneven potential distribution with severe polarization, whereas S-PEO shows relatively uniform potential distribution with mitigated surface polarization. L-PEO, in comparison, demonstrates the most uniform potential distribution with negligible polarization at the electrode surface.

The conclusions drawn from the above characterization and simulations are further validated through SEM morphological analysis of the sodium metal surface after 50 charge–discharge cycles in the Na|ASSE|Na configuration. As shown in Fig. S13a, the Na anode adjacent to P-PEO (stripping side) displays distinct surface cracks following sodium stripping from the surface layer, indicating structural collapse of the sodium anode after repeated stripping. In contrast, while NaF incorporation effectively alleviates surface cracking of the Na anode (Fig. S13b), long-term non-uniform sodium deposition still results in relatively rough anode morphology—potentially triggering dendrite propagation and compromising cycling stability. For L-PEO, however, the corresponding Na surface exhibits a remarkably flat, smooth, and dense morphology (Fig. S13c), demonstrating that LiF addition not only mitigates cracking during stripping but also promotes compact sodium deposition through regulated displacement reactions at the anode interface.

The stabilizing effect of reactive fluorides on sodium anode performance is more pronounced in the top-view and cross-sectional SEM images of the deposition side (Fig. 4j–l). Pristine P-PEO exhibits rough deposits with spherical sodium crystals of varying sizes, confirming unstable deposition behavior (Fig. 4j). Repeated cycling exacerbates this morphological heterogeneity, potentially inducing non-uniform dendrite growth and increasing the risk of electrolyte penetration. While NaF addition suppresses side reactions during sodium deposition—particularly dendrite nucleation and growth—the resulting sodium surface remains uneven with

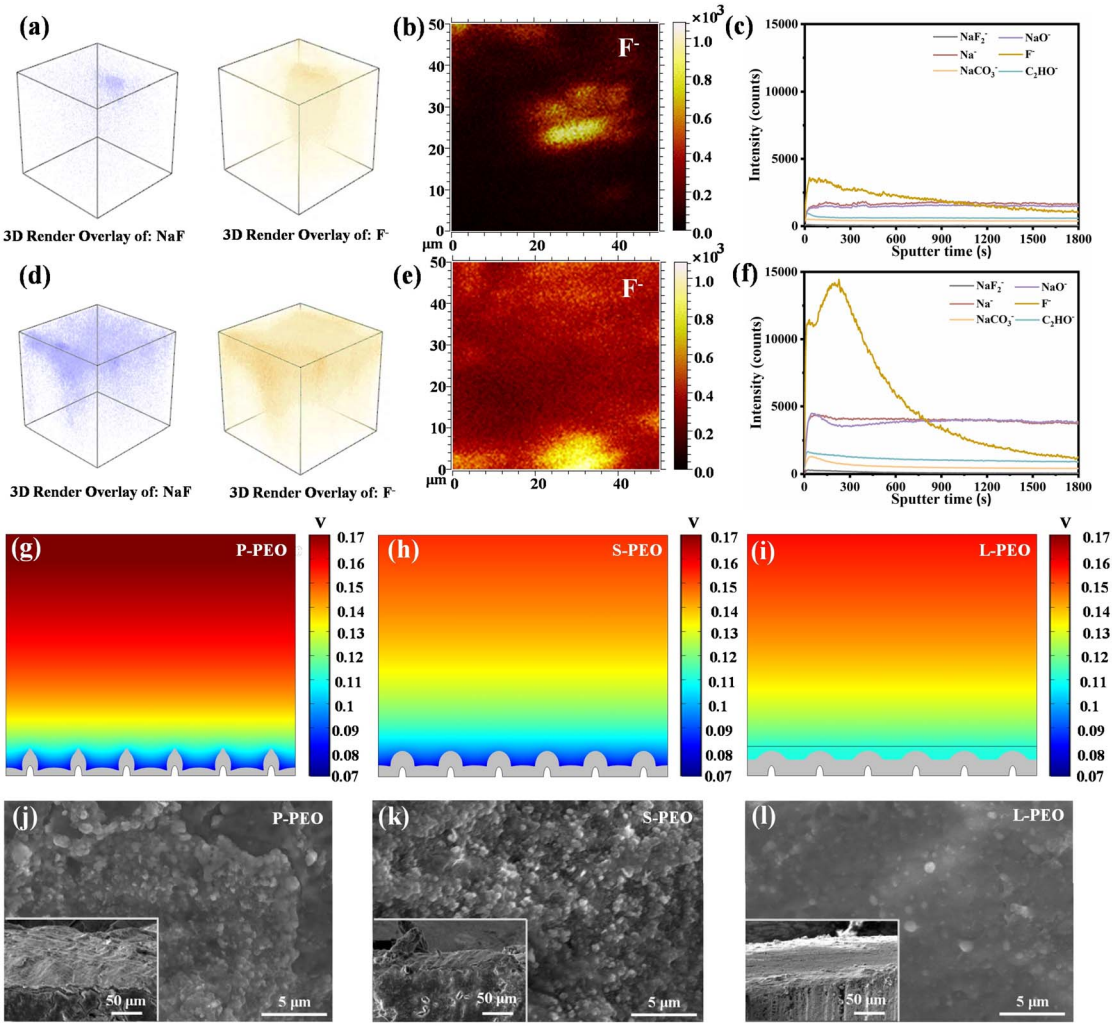

Fig. 4 Characterization of the structure and composition distribution at the electrode interface and finite element analysis. 3D reconstructed TOF-SIMS images of NaF and F^- at the (a) Na/P-PEO and (d) Na/L-PEO interface. TOF-SIMS F^- mapping images of (b) P-PEO and (e) L-PEO. TOF-SIMS depth profiles of various compositions formed at (c) Na/P-PEO and (f) Na/L-PEO interfaces after cell cycling. The potential distribution map obtained through FEA of (g) P-PEO, (h) S-PEO and (i) L-PEO. SEM images of Na after cycling in (j) Na|P-PEO|NVP, (k) Na|S-PEO|NVP, and (l) Na|L-PEO|NVP cells (Na deposition) with the corresponding cross-sectional diagram shown in insets in each figure.

visible cracks due to insufficient anode protection and deposition guidance (Fig. 4k). In striking contrast, the sodium anode adjacent to L-PEO displays a uniformly dense surface (Fig. 4l), which arises from LiF reacting with surface sodium to form a continuous NaF protective layer through displacement reactions, thereby guiding uniform deposition and inhibiting dendrite formation.

Leveraging bulk-phase intermolecular interactions and an interfacial buffer layer constructed *via* reactive fluorides, L-PEO demonstrates substantial advantages in electrochemical performance. *In situ* EIS measurements combined with corresponding distribution of relaxation time (DRT) analysis were employed to further verify the stability of ASSEs during battery cycling, with a primary focus on observing sodium ion transport and conversion behavior in Na|ASSE|NVP batteries across various states of charge during the first cycle. As shown in Fig. 5a–g, the main relaxation time signals of the impedance of the corresponding Na|ASSE|NVP batteries can be categorized into three regions, which are R_b representing ohmic resistance ($\tau \approx 10^{-6}$ s), $R_{SEI/CEI}$ representing solid electrolyte interphase/cathode electrolyte interphase (SEI/CEI) resistance ($\tau = 10^{-4}$ to 10^{-2} s), and R_{CT} representing charge transfer resistance ($\tau > 10^{-2}$ s).[55–57] The first charging process of the system involves the formation of a stable SEI/CEI on the electrode surface and the establishment of stable Na^+-conducting pathways in the electrolyte bulk phase. As shown in Fig. 5g and S14, the Na|L-PEO|NVP battery exhibits a lower R_{CT} compared to the Na|P-PEO|NVP and Na|S-PEO|NVP batteries during charging, indicating superior transport kinetics at the Na anode–electrolyte interface, with this difference becoming even more pronounced during discharge (Fig. 5d–f and S15). The DRT plots (Fig. S15) track impedance evolution during charging: at 3.8 V (post-charging), L-PEO shows a marked increase in the intensity of the long relaxation time ($\tau \sim 10^{-1}$ to 10^{0} s) peak (interfacial

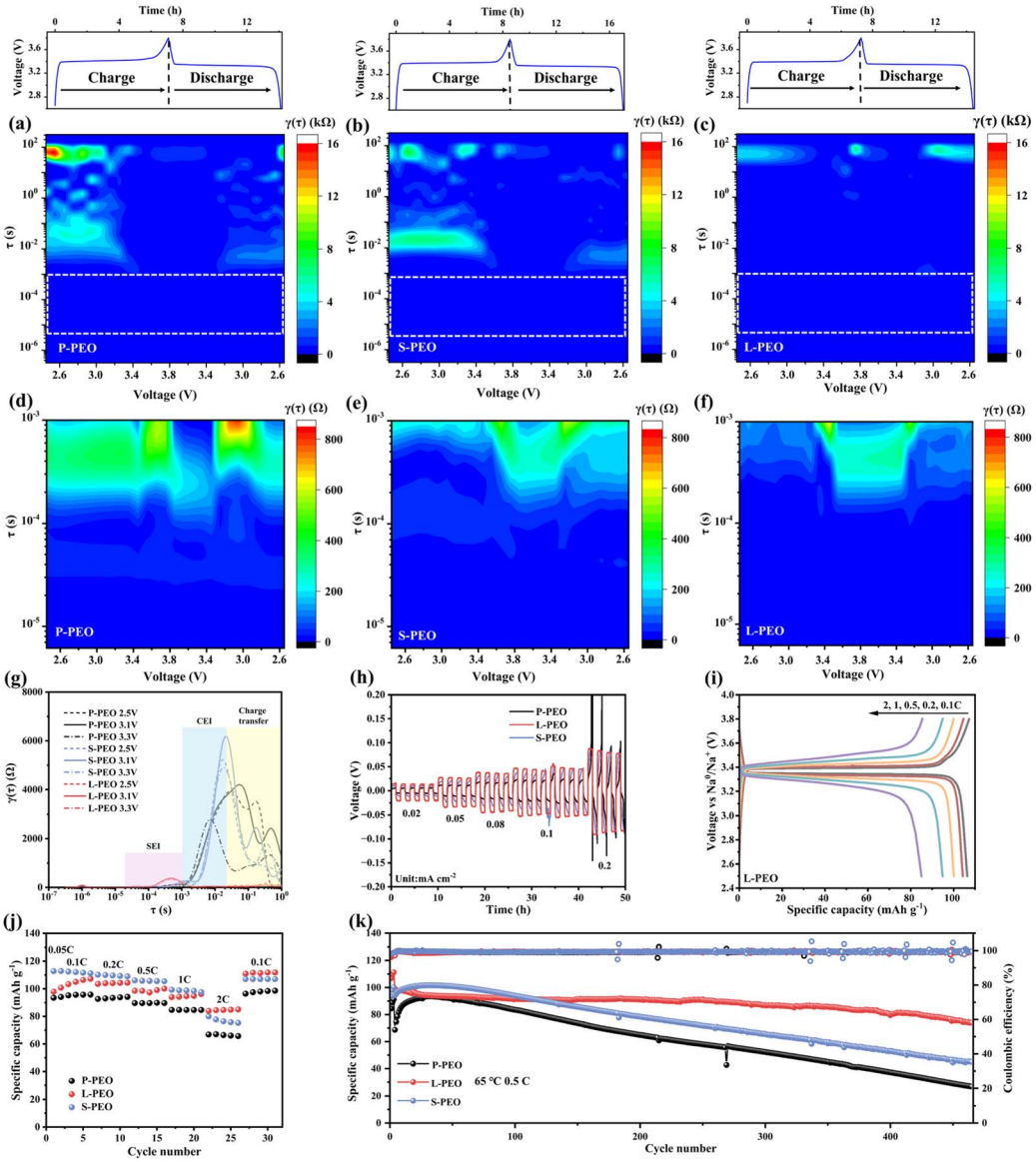

Fig. 5 The interfacial stability and electrochemical performance of PEO-based Na batteries. Distribution of relaxation time (DRT) intensity color maps of NVP||Na cells employing (a), (d) P-PEO, (b), (e) S-PEO, and (c), (f) L-PEO at various potentials during cycling at 65 °C, and (d)–(f) present the enlarged view of the area outlined by the dashed rectangle in (a)–(c), respectively. (g) The DRT curves of NVP||Na cells with P-PEO, S-PEO and L-PEO at different charging voltages. (h) Critical current density (CCD) tests (at increased current densities ranging from 0.02 to 0.2 mA cm^{-2}). (i) Voltage profiles of NVP||Na cells with L-PEO. (j) Rate performance and (k) cycling performance of NVP-based ASSLBs. All electrochemical tests were performed at 65 °C.

processes) compared to 2.5 V (pre-charging), indicating rising interfacial impedance with charging. This impedance elevation directly stems from the gradual formation of a compact, NaF-rich SEI layer at the electrode–electrolyte interface. Notably, however, the Na|L-PEO|NVP battery exhibits a slightly higher R_{SEI} than the others, which is associated with its unique LiF-induced SEI formation mechanism. LiF, which undergoes supramolecular coordination with PEO segments, exhibits enhanced reactivity and readily undergoes an *in situ* replacement reaction at the sodium metal surface. The uniformly distributed NaF generated from this *in situ* reaction acts as a heterogeneous nucleation site on the anode surface, effectively reducing the surface energy for Na deposition. This process facilitates the formation of a more compact NaF-rich SEI layer. Although this denser SEI layer initially exhibits a relatively higher R_{SEI} (*i.e.*, interface resistance), it demonstrates a superior physical barrier effect and more ordered ion transport pathways during prolonged electrochemical cycling, thereby leading to significantly enhanced interfacial stability.

The promotion of stable Na^+ transport by the reactive fluoride-induced dynamic bulk phase/interfacial regulation of the solid-state systems can be further confirmed by the sodium deposition and stripping performance at different current densities. Critical current density (CCD) tests with applied

current density increased from 0.02 to 0.2 mA cm^{-2} were performed in Na|ASSE|Na symmetric cells (1 h of stripping and 1 h of plating, Fig. 5h). Although L-PEO exhibits slightly higher overpotential at lower current densities, it retains the most stable stripping/plating performance even at 0.2 mA cm^{-2}. This superiority arises from its enhanced bulk Na^+ conductivity and the formation of a NaF-rich interfacial layer. In contrast, P-PEO and S-PEO suffer from markedly escalating overpotentials and interfacial instability with increasing current density, attributed to uneven Na deposition and persistent interfacial degradation. The long-cycle stability of symmetric Na||Na cells utilizing L-PEO (Fig. S16) further attests to its superior performance.

Na||NVP batteries utilizing PEO-based electrolytes were evaluated at various rates at 65 °C. As shown in Fig. S17a, Na|P-PEO|NVP delivered specific capacities of 94.1 mAh g^{-1}, 92.7 mAh g^{-1}, 89.7 mAh g^{-1}, 84.7 mAh g^{-1}, and 66.8 mAh g^{-1}, respectively, as the discharging rate changes from 0.1C to 2.0C with the capacity retention at 2.0C being 71.1%. Benefiting from the optimized polymer segment mobility, S-PEO exhibits a higher initial discharge capacity (112.9 mAh g^{-1} at 0.1C) and a higher capacity retention rate at high rates (71.9% at 2C), as shown in Fig. 5j and S17b. Due to the presence of a denser SEI layer, Na|L-PEO|NVP shows a more obvious activation process during the initial charge–discharge process. During the first five cycles of the 0.1C cycling, the discharge capacity gradually increases from 100.8 mAh g^{-1} to 107.2 mAh g^{-1}. When the activation process is completed, L-PEO shows excellent interfacial stability and delivers a specific capacity of 84.0 mAh g^{-1} at 2.0C, representing a capacity retention of 85.8% (Fig. 5i and j). The superior performance of L-PEO may stem from LiF reacting preferentially with sodium metal at the interface during charge–discharge cycles, forming a stable SEI layer containing NaF. The uniform distribution of NaF and organic components ensures rapid sodium ion diffusion within the SEI layer and maintains a stable interface. To further evaluate the interface stability of both electrolyte membranes toward sodium metal, the long-term cycling performance of symmetric cells was investigated to assess LiF's effect on suppressing sodium dendrite growth in PEO-based polymer electrolyte. The Na|L-PEO|NVP battery demonstrates exceptional long-term cycling stability, as illustrated in Fig. 5k. After 400 cycles at 0.5C, it retains a reversible discharge capacity of 79.8 mAh g^{-1} with a capacity retention of 82.8%, which can be attributed to the stable Na|L-PEO interface. In contrast, the Na|P-PEO|NVP and Na|S-PEO|NVP batteries exhibit significantly inferior performance, delivering only 36.9 mAh g^{-1} and 52.3 mAh g^{-1} after 400 cycles at 0.5C with 55.2% and 56.0% capacity retention, respectively, which is likely due to the unstable Na|P-PEO and Na|S-PEO interface and poor ionic conductivity.

Conclusions

This work demonstrates a reactive fluoride-mediated strategy to simultaneously enhance bulk ion transport and interfacial stability in PEO-based ASSMBs. Compounds formed through supramolecular interactions among LiF, PEO and OTf^- enable weakened Na^+–polymer coordination and the formation of immobilized anions in the bulk phase, while a uniform NaF-rich SEI for dendrite suppression is constructed through supramolecular interaction-assisted *in situ* displacement reactions. The modified electrolyte exhibits improved ionic conductivity, mechanical strength, and interfacial compatibility. As a result, all-solid-state Na cells employing the LiF-modified electrolyte achieve superior rate capability and exceptional long-term cycling stability. This work underscores the critical role of reactive fluoride-mediated supramolecular compounds in enabling dynamic bulk and interfacial regulation, offering a promising design strategy for high-performance and safe polymer-based solid-state batteries.

Author contributions

Y. Fan and B. Zhao contributed equally to this work. Y. Tang and Y. Fan proposed the idea for this work and designed the experiments. B. Zhao and X. Zou performed material preparation, characterization, and electrochemical measurements. W. Zhao and Y. Shen provided resources. M. Zhu and Z. Hong were responsible for figure preparation and data visualization. X. Cheng and P. Chen conducted data curation. Z. Bai and H. Zhang carried out the investigation. Y. Zhang contributed to conceptualization. Y. Tang supervised the research, acquired funding, administered the project, and revised the manuscript. Y. Fan and B. Zhao wrote the original draft. The manuscript was discussed and revised by all authors.

Conflicts of interest

There are no conflicts to declare.

Data availability

The data that support the findings of this study are available within the article and its supplementary information (SI) or from the corresponding author on reasonable request.

Supplementary information: the experimental details, basic morphological and mechanical characterizations, as well as electrochemical performances. See DOI: https://doi.org/10.1039/d5sc08784h.

Acknowledgements

The authors acknowledge financial support from the National Natural Science Foundation of China (22279017) and the National Key R&D Program of China (2024YFE0101600). This work was also supported by the Platform Supporting Fund of Qingyuan Innovation Laboratory (Grant No. 00623001), Startup Fund of Qingyuan Innovation Laboratory (Grant No. 00524009), and Key Program of Qingyuan Innovation Laboratory (Grant No. 00223002).

Notes and references

1 X. Wang, C. Zhang, M. Sawczyk, J. Sun, Q. Yuan, F. Chen, T. C. Mendes, P. C. Howlett, C. Fu, Y. Wang, X. Tan,

D. J. Searles, P. Král, C. J. Hawker, A. K. Whittaker and M. Forsyth, *Nat. Mater.*, 2022, **21**, 1057–1065.
2 Z. Chen, Z. Yang, X. Tan, Y. Wang, B. Luo, X. Wang, M. Forsyth, C. J. Hawker, D. J. Searles and C. Zhang, *J. Am. Chem. Soc.*, 2025, **147**, 28464–28473.
3 W. Tian, G. Lin, S. Yuan, T. Jin, Q. Wang and L. Jiao, *Angew. Chem., Int. Ed.*, 2025, **64**, e202423075.
4 F. Ling, J. Diao, Y. Yao, R. Bai, Z. Li, M. Ma, Z. Li, H. Huang, S. Zhu, X. Rui, Y. Shao, G. Henkelman and Y. Yu, *Adv. Funct. Mater.*, 2025, **35**, 2419970.
5 X. Chen, X. Zhou, Z. Yang, Z. Hao, J. Chen, W. Kuang, X. Shi, X. Wu, L. Li and S. Chou, *Chem. Sci.*, 2024, **15**, 4833–4838.
6 X. Yu, L. Xue, J. B. Goodenough and A. Manthiram, *ACS Mater. Lett.*, 2019, **1**, 132–138.
7 T. Han, Z. Cui, W. Kuang, Y. Cai, J. Sun and Y. Y. Li, *Adv. Funct. Mater.*, 2025, e13625.
8 L. Dai, M. Cai, X. Zhou, W. Liang, Z. Zhao, Z. Xia, F. Huang, J. Jiang, W. Jiang, B. Zhang and Z. Ma, *Chem. Sci.*, 2025, **16**, 2453–2464.
9 S. Dwivedi, S. Vasudevan and P. Balaya, *J. Mater. Chem. A*, 2024, **12**, 22867–22882.
10 S. Pathreeker, C. A. Snyder, G. V. Papamokos and R. J. Composto, *Chem. Mater.*, 2024, **36**, 7843–7856.
11 S. Chen, Z. Wei, C. Bai, S. Niu and W. Wei, *Chem. Eng. J.*, 2023, **472**, 145140.
12 A. Helaley and X. Liang, *Chem. Eng. J.*, 2025, **514**, 163173.
13 O. Chiekezi, X. He, H. Wang, T. R. Adebisi, O. Ayodele, T. Deng, D. Reed, C. Wang and X. Lu, *ACS Appl. Energy Mater.*, 2023, **6**, 8434–8442.
14 R. Liao, C. Li, M. Zhou, R. Liu, S. Liu and D. Wu, *Chem. Sci.*, 2024, **15**, 18327–18334.
15 K. G. Stakem, F. J. Leslie and G. L. Gregory, *Chem. Sci.*, 2024, **15**, 10281–10307.
16 Q. Zhou, J. Ma, S. Dong, X. Li and G. Cui, *Adv. Mater.*, 2019, **31**, 1902029.
17 H. Tu, Y. Zhang, J. Wu, Y. Li, H. Liu, W. Deng, G. Zou, H. Hou and X. Ji, *Adv. Funct. Mater.*, 2024, **35**, 2413488.
18 L. Brunsveld, B. J. B. Folmer, E. W. Meijer and R. P. Sijbesma, *Chem. Rev.*, 2001, **101**, 4071–4097.
19 G. Chen, Y. Bai, Y. Gao, Z. Wang, K. Zhang, Q. Ni, F. Wu, H. Xu and C. Wu, *ACS Appl. Mater. Interfaces*, 2019, **11**, 43252–43260.
20 S. Bublil, G. Peta, H. Alon-Yehezkel, Y. Elias, D. Golodnitsky, M. Fayena-Greenstein and D. Aurbach, *J. Electrochem. Soc.*, 2022, **169**, 020504.
21 V. Iyer, J. Petersen, S. Geier and P. Wierach, *Polymers*, 2024, **16**, 2806.
22 C. Ma, K. Dai, H. Hou, X. Ji, L. Chen, D. G. Ivey and W. Wei, *Adv. Sci.*, 2018, **5**, 1700996.
23 G. Peta, H. Alon-Yehezkel, N. R. Samala, S. Bublil, Y. Elias, I. Grinberg, M. Fayena-Greenstein and D. Aurbach, *J. Electrochem. Soc.*, 2023, **170**, 090516.
24 H. Chen, H. Zang, J. Du, H. Zhang, X. Xu, P. Zhang, X. Li, J. Han, X. Li and Q. Wang, *Adv. Funct. Mater.*, 2025, **35**, 2504177.
25 S. Qu, G. Cai, X. Qiao, G. Li and J. Sun, *ACS Appl. Energy Mater.*, 2024, **7**, 8964–8972.
26 Y. Lu, L. Li, Q. Zhang, Y. Cai, Y. Ni and J. Chen, *Chem. Sci.*, 2022, **13**, 3416–3423.
27 J. Wu, Z. Yu, Q. Wang and X. Guo, *Energy Storage Mater.*, 2020, **24**, 467–471.
28 L. Liu, X. Qi, S. Yin, Q. Zhang, X. Liu, L. Suo, H. Li, L. Chen and Y. Hu, *ACS Energy Lett.*, 2019, **4**, 1650–1657.
29 X. Xu, Y. Li, J. Cheng, G. Hou, X. Nie, Q. Ai, L. Dai, J. Feng and L. Ci, *J. Energy Chem.*, 2020, **41**, 73–78.
30 X. Yu, L. Xue, J. B. Goodenough and A. Manthiram, *Adv. Funct. Mater.*, 2020, **31**, 2002144.
31 C. Peng, S. Huang, X. Shen, J. Ding, J. Luo, J. Du, Z. Xia, X. Zhang and J. Chen, *J. Mater. Chem. A*, 2024, **12**, 23485–23494.
32 P. Kumari, A. Kumar, H. Lohani, A. Ahuja, A. Sengupta and S. Mitra, *ACS Appl. Mater. Interfaces*, 2025, **17**, 30793–30805.
33 G. Homann, L. Stolz, K. Neuhaus, M. Winter and J. Kasnatscheew, *Adv. Funct. Mater.*, 2020, **30**, 2006289.
34 X. Yang, M. Jiang, X. Gao, D. Bao, Q. Sun, N. Holmes, H. Duan, S. Mukherjee, K. Adair, C. Zhao, J. Liang, W. Li, J. Li, Y. Liu, H. Huang, L. Zhang, S. Lu, Q. Lu, R. Li, C. V. Singh and X. Sun, *Energy Environ. Sci.*, 2020, **13**, 1318–1325.
35 S. F. Wen, Z. F. Sun, X. Y. Wu, S. H. Zhou, Q. Z. Yin, H. Y. Chen, J. H. Pan, Z. W. Zhang, Z. L. Zhuang, J. Y. Wan, W. D. Zhou, D. L. Peng and Q. B. Zhang, *Adv. Funct. Mater.*, 2025, **35**, 2422147.
36 X. Han, L. H. Gu, Z. F. Sun, M. F. Chen, Y. G. Zhang, L. S. Luo, M. Xu, S. Y. Chen, H. D. Liu, J. Y. Wan, Y. B. He, J. Z. Chen and Q. B. Zhang, *Energy Environ. Sci.*, 2023, **16**, 5395–5408.
37 Z. F. Sun, Q. Z. Yin, H. Y. Chen, M. Li, S. H. Zhou, S. F. Wen, J. H. Pan, Q. Z. Zheng, B. Jiang, H. D. Liu, K. Kim, J. Li, X. Han, Y. B. He, L. Zhang, M. C. Li and Q. B. Zhang, *Interdiscip. Mater.*, 2023, **2**, 635–663.
38 X. Zhan, M. Li, X. L. Zhao, Y. N. Wang, S. Li, W. W. Wang, J. D. Lin, Z. A. Nan, J. W. Yan, Z. F. Sun, H. D. Liu, F. Wang, J. Y. Wan, J. J. Liu, Q. B. Zhang and L. Zhang, *Nat. Commun.*, 2024, **15**, 1056.
39 B. Han, Y. Zou, Z. Zhang, X. Yang, X. Shi, H. Meng, H. Wang, K. Xu, Y. Deng and M. Gu, *Nat. Commun.*, 2021, **12**, 3066.
40 H. An, M. Li, Q. Liu, Y. Song, J. Liu, Z. Yu, X. Liu, B. Deng and J. Wang, *Nat. Commun.*, 2024, **15**, 9150.
41 J. Hu, C. Lai, K. Chen, Q. Wu, Y. Gu, C. Wu and C. Li, *Nat. Commun.*, 2022, **13**, 7914.
42 Y. Fan, O. I. Malyi and Y. Tang, *Sci. China Mater.*, 2025, DOI: 10.1007/s40843-025-3590-8.
43 L. Wang, Y. Zhong, Z. Wen, C. Li, J. Zhao, M. Ge, P. Zhou, Y. Zhang, Y. Tang and G. Hong, *Sci. China Mater.*, 2022, **65**, 2179–2188.
44 A. Vila, J. M. Pardo and R. A. Mosquera, *Chem. Phys. Lett.*, 2003, **375**, 499–505.
45 R. Andersson, G. Hernández and J. Mindemark, *Phys. Chem. Chem. Phys.*, 2022, **24**, 16343–16352.
46 B. K. Rao, R. Singh and M. L. Verma, *Polym. Bull.*, 2021, **78**, 1441–1452.
47 M. Akhtar, S. K. Pradhan, J. Chang and S. B. Majumder, *ACS Sustainable Chem. Eng.*, 2020, **8**, 7523–7535.

48 M. Akhtar and S. B. Majumder, *ACS Appl. Energy Mater.*, 2021, **4**, 13538–13549.
49 R. L. Karlinsey, L. M. Bronstein and J. W. Zwanziger, *J. Phys. Chem. B*, 2004, **108**, 918–928.
50 Y. Fan, O. I. Malyi, H. Wang, X. Cheng, X. Fu, J. Wang, H. Ke, H. Xia, Y. Shen, Z. Bai, S. Chen, H. Shao, X. Chen, Y. Tang and X. Bao, *Angew. Chem., Int. Ed.*, 2025, **64**, e202421777.
51 C. Liu and H. Chen, *Macromolecules*, 2017, **50**, 631–641.
52 S. Kirkham, V. Castelletto, I. W. Hamley, M. Reza, J. Ruokolainen, D. Hermida-Merino, P. Bilalis and H. Iatrou, *Biomacromolecules*, 2016, **17**, 1186–1197.
53 C. P. Rhodes and R. F. Frech, *Solid State Ionics*, 1999, **121**, 91–99.
54 W. Zhang, Q. Lu, G. Sun, Z. Chen, P. Yue, G. Zhang, B. Song and K. Song, *Nano Lett.*, 2025, **25**, 6092–6100.
55 Z. Li, H. Wang, Y. Zheng, Y. Zhu, B. Qin, Z. Lu, W. Yan and J. Zhang, *Angew. Chem., Int. Ed.*, 2025, **64**, e202508857.
56 X. Qin, L. Zhao, J. Han, J. Xiao, Y. Wang, C. Ji, T. Liu, M. Zuo, J. Sun, D. Kong, M. Wu, W. Lv, Q. Yang and L. Zhi, *ACS Nano*, 2025, **19**, 17760–17773.
57 Y. Lu, C. Z. Zhao, J. Q. Huang and Q. Zhang, *Joule*, 2022, **6**, 1172–1198.